

# Nonlinear mechanism of the self-sustaining process in the buffer and logarithmic layer of wall-bounded flows

H. Jane Bae<sup>1,†</sup>, A. Lozano-Durán<sup>2</sup> and Beverley J. McKeon<sup>1</sup>

<sup>1</sup>Graduate Aerospace Laboratories, California Institute of Technology, Pasadena, CA 91125, USA

<sup>2</sup>Center for Turbulence Research, Stanford University, Stanford, CA 94305, USA

(Received 14 April 2020; revised 26 September 2020; accepted 5 October 2020)

The nonlinear mechanism in the self-sustaining process (SSP) of wall-bounded turbulence is investigated. Resolvent analysis is used to identify the principal forcing mode that produces the maximum amplification of the velocities in numerical simulations of the minimal channel for the buffer layer and a modified logarithmic (log) layer. The wavenumbers targeted in this study are those of the fundamental mode, which is infinitely long in the streamwise direction and once-periodic in the spanwise direction. The identified mode is then projected out from the nonlinear term of the Navier–Stokes equations at each time step from the simulation of the corresponding minimal channel. The results show that the removal of the principal forcing mode of the fundamental wavenumber can inhibit turbulence in both the buffer and log layer, with the effect being greater in the buffer layer. Removing other modes instead of the principal mode of the fundamental wavenumber only marginally affects the flow. Closer inspection of the dyadic interactions in the nonlinear term shows that contributions to the principal forcing mode come from a limited set of wavenumber interactions. Using conditional averaging, the flow structures that are responsible for generating the nonlinear interaction to self-sustain turbulence are identified as spanwise rolls interacting with oblique streaks. This method, based on the equations of motion, validates the similarities in the SSP of the buffer and log layer, and characterises the underlying quadratic interactions in the SSP of the minimal channel.

**Key words:** turbulent boundary layers, turbulence theory

† Email address for correspondence: [hjbae@caltech.edu](mailto:hjbae@caltech.edu)

## 1. Introduction

Since the first experiments by Klebanoff, Tidstrom & Sargent (1962) and Kline *et al.* (1967), the coherent structure of near-wall turbulence has been extensively investigated. In the vicinity of the wall, the flow is found to be highly organised and can be comprehended as a collection of recurrent patterns usually referred to as coherent structures or eddies, consisting of streamwise rolls/vortices and low- and high-speed streaks (Kline *et al.* 1967; Blackwelder & Eckelmann 1979; Smith & Metzler 1983), that are involved in a quasi-periodic regeneration cycle (Robinson 1991; Panton 2001; Adrian 2007). However, despite the large efforts devoted to the subject, questions still remain regarding the exact mechanisms by which turbulence self-sustains in wall-bounded turbulent shear flows and the dynamics in which these structures interact.

Townsend (1976) hypothesised that the log region would be composed of self-similar energy-containing motions, the sizes of which are proportional to their distance from the wall. By a suitable superposition of these hypothetical motions, termed ‘attached eddies’, under the constraint of a constant Reynolds shear stress typical of the log layer, Townsend predicted that the wall-parallel velocity components of turbulence intensities in the log region would exhibit logarithmic wall-normal dependence. Traditionally, wall-attached eddies have been interpreted as statistical entities (Marusic *et al.* 2010; Smits, McKeon & Marusic 2011), but recent works suggest that they can also be identified as instantaneous features of the flow (Jiménez 2018). The methodologies to identify instantaneous energy eddies are diverse and frequently complementary, ranging from the Fourier characterisation of the turbulent kinetic energy (Jiménez 2013, 2015) to adaptive mode decomposition (Hellström, Ganapathisubramani & Smits 2016; Agostini & Leschziner 2019; Cheng *et al.* 2019), and three-dimensional clustering techniques (Del Alamo & Jiménez 2006; Lozano-Durán, Flores & Jiménez 2012; Lozano-Durán & Jiménez 2014; Hwang & Sung 2018), to name a few.

In the buffer layer, important progress was made in the early 1990s using the ‘minimal flow unit’ approach, which revealed that buffer-layer streaks can self-sustain even when motions at larger scales are inhibited and that their existence, therefore, relies on an autonomous process (Jiménez & Moin 1991). Hamilton, Kim & Waleffe (1995) utilised a similar approach for Couette flow, where either certain velocity modes were suppressed to remove streak formation or disturbances were added to allow streak breakdown. Jiménez & Pinelli (1999) further confirmed that this near-wall process is independent of the flow in the log and outer regions by showing the survival of the near-wall motions in the absence of outer turbulence. The consensus from these studies, along with many others that followed (e.g. Waleffe 1997; Schoppa & Hussain 2002; Farrell, Gayme & Ioannou 2017), is that the streaks are significantly amplified by the quasi-streamwise vortices via the lift-up effect (Landahl 1975); the amplified streaks subsequently undergo a rapid streamwise meandering motion, reminiscent of streak instability or transient growth, which eventually results in the breakdown of the streaks and regeneration of new quasi-streamwise vortices (Swearingen & Blackwelder 1987; Waleffe 1995; Kawahara *et al.* 2003). The cycle is restarted by the generation of new vortices from the perturbations created by the disrupted streaks through nonlinear interactions.

A similar but more disorganised scenario is hypothesised to occur for the larger wall-attached energy eddies within the log layer (Flores & Jiménez 2010; Hwang & Cossu 2011; Cossu & Hwang 2017; Lozano-Durán, Bae & Encinar 2020). The existence of a self-similar streak/roll structure in the log layer consistent with Townsend’s attached-eddy model has been supported by the numerical studies by Del Alamo & Jiménez (2006), Flores & Jiménez (2010), Hwang & Cossu (2011), Lozano-Durán *et al.* (2012) and Lozano-Durán & Jiménez (2014), among others. A growing body of evidence also

indicates that the generation of the log-layer streaks has its origins in the linear lift-up effect (Kim & Lim 2000; Del Alamo & Jiménez 2006; Pujals *et al.* 2009; Hwang & Cossu 2010; Moarref *et al.* 2013; Alizard 2015) in conjunction with Orr's mechanism (Orr 1907; Jiménez 2012). Regarding roll formation, several works have speculated that rolls are the consequence of a sinuous secondary instability of the streaks that collapse through a rapid meander until breakdown (Andersson *et al.* 2001; Park, Hwang & Cossu 2011; Alizard 2015; Cassinelli, de Giovanetti & Hwang 2017), while others advocate for transient growth (Schoppa & Hussain 2002) or parametric instability of the streamwise-averaged mean flow as the generating mechanism of the rolls (Farrell *et al.* 2016).

The specific mechanism by which the coherent large-scale structures self-sustain can be further investigated by looking for the existence of invariant solutions of the Navier–Stokes equations (Waleffe 1998, 2001, 2003). The nonlinear steady-state solutions and travelling wave solutions in plane Couette flow and the travelling wave solutions in plane Poiseuille flow, also known as exact coherent structures (ECS), are a combination of the three flow structures – streamwise vortices, streaks and waves – such that they maintain each other despite viscous decay. The idea was that these ECS act as an organising centre for the turbulence quasi-cycle. Kawahara & Kida (2001) detected periodic orbits resembling the time-dependent version of Waleffe's self-sustaining process (SSP) that shares the full regeneration cycle of the near-wall coherent structures in plane Couette turbulence. Further study was done in the large-scale motions (Cossu & Hwang 2017) using over-damped large-eddy simulation to isolate the large-scale motions. However, while realistic turbulence does show similarity to ECS solutions, the actual dynamics of wall-bounded turbulence exhibits more complexity than the ones observed in ECS.

Several mechanisms for vortex regeneration have been proposed in the past, mostly focused on the buffer region (Jiménez & Moin 1991; Hamilton *et al.* 1995; Panton 1997; Schoppa & Hussain 2002; Hwang & Bengana 2016) due to the fundamentally nonlinear nature of the problem. Previous studies successfully identified the dominant wavenumbers involved in the nonlinear interaction (Hamilton *et al.* 1995) and the structures involved in the regeneration mechanism based on instantaneous snapshots of turbulent flow (Jiménez & Moin 1991; Hamilton *et al.* 1995; Schoppa & Hussain 2002). However, additional insight is necessary to pinpoint the exact nonlinear interaction involved in the regeneration cycle, i.e. to understand the underlying flow composition that leads to the meaningful nonlinear interaction that produces the structures involved in the SSP, in realistic turbulent flows. A meaningful addition to the previous studies would be to find an orthonormal basis for the nonlinear term of the Navier–Stokes equations that isolates the most important nonlinear interaction leading to regeneration of streamwise vortices, which is the goal of the present study.

Various approaches rooted in the linearised equations have been utilised in the past to study turbulent flows, such as rapid distortion theory of Batchelor & Proudman (1954) (see the reviews by Hunt & Carruthers (1990) and Cambon & Scott (1999) for more details), linear stability theory (Lin 1944; Malkus 1956; Reynolds & Hussain 1972), optimal perturbation (Butler & Farrell 1993; Farrell & Ioannou 1993), input–output analysis (Jovanovic & Bamieh 2005) and resolvent analysis (McKeon & Sharma 2010; McKeon 2017), among others. Early works focused their efforts on transition to turbulence, while more recent studies have been devoted to fully turbulent flows. Here we focus on the latter using resolvent analysis, as it has been successful at identifying the most energetic motions in actual turbulent flows by approximating the nonlinear forcing from the interaction of highly amplified coherent structures (McKeon & Sharma 2010; McKeon 2017). Resolvent analysis identifies pairs of response (velocity) and forcing (nonlinear) modes and the

corresponding amplification factor from the linearised Navier–Stokes operator while taking into account the non-normality of the linear Navier–Stokes equations. This results in a set of orthonormal bases for the velocity and nonlinear terms. A more detailed comparison of previous works on linearised Navier–Stokes equations with the resolvent analysis can be found in McKeon (2017).

It has been shown that a rank-one approximation of the resolvent modes captures the characteristics of the most energetic modes of wall-bounded turbulent channels (Moarref *et al.* 2013). We postulate that the principal (most amplified) forcing mode then must have the largest impact on the flow and, in particular, the regeneration cycle, and we show that the turbulence can be weakened by removing the nonlinear component corresponding to the principal forcing mode in both the buffer and the log layer. The orthonormality of the resolvent modes allows the removal of the spatio-temporal structure corresponding to the principal forcing mode by extracting the projection of forcing mode onto the nonlinear term. Furthermore, by identifying the most important contribution to the nonlinear term, conditional averaging can identify the underlying interaction that leads to the generation of this nonlinear term, making it possible to study the structures responsible for the nonlinear mechanism in the SSP. A preliminary version of this work can be found in Bae & McKeon (2020).

The paper is organised as follows. We first introduce the method used to identify and remove resolvent forcing modes from the nonlinear term computed from the numerical simulations of low- and moderate-Reynolds-number minimal channel flow simulations, representing the buffer and log-layer dynamics, in § 2. We then present the resulting changes in the flow statistics once the resolvent forcing modes are projected out in § 3, where it is shown that the removal of the principal forcing modes can significantly reduce turbulence in both the buffer and log layers. The precursor velocity structures involved in the generation of the most amplified nonlinear term, and thus the structures involved in the nonlinear mechanisms of the SSP, are identified in § 4. Finally, our findings are summarised in § 5.

## 2. Methods

In the following, we consider a turbulent flow between two parallel walls. The streamwise, wall-normal and spanwise directions are denoted by  $x$ ,  $y$  and  $z$ , respectively. The streamwise and spanwise directions are periodic. The flow velocities in the corresponding directions are given by  $\bar{U}$ ,  $\bar{V}$  and  $\bar{W}$ . We define two decompositions of the flow velocities,  $\bar{U} = U + u = \bar{u} + u'$ , where  $U$  is the velocity averaged over the homogeneous directions and time, and  $\bar{u}$  is the velocity averaged over the homogeneous directions only (analogously defined for  $\bar{V}$  and  $\bar{W}$ ). The flow is characterised by the friction Reynolds number  $Re_\tau = \delta u_\tau / \nu$ , where  $\delta$  is the channel half-height,  $u_\tau$  is the friction velocity and  $\nu$  is the kinematic viscosity.

### 2.1. Principal forcing modes

In order to identify the most amplified nonlinear component in the turbulent channel flow, we perform the resolvent analysis with the base mean flow being the mean velocity of a turbulent channel flow,  $U = (U, V, W)$ . The incompressible Navier–Stokes equations can be Fourier-transformed in homogeneous directions and time, and reorganised as

$$-i\omega\tilde{u} + (U \cdot \hat{\nabla})\tilde{u} + (\tilde{u} \cdot \hat{\nabla})U + \hat{\nabla}\tilde{p} - \frac{1}{Re_\tau}\hat{\Delta}\tilde{u} = \tilde{f}, \quad \hat{\nabla} \cdot \tilde{u} = 0, \quad (2.1)$$

for each  $(k_x, k_z, \omega) \neq (0, 0, 0)$ , where  $(\tilde{\cdot})$  is the Fourier transform in time and space,  $\tilde{\mathbf{u}}(k_x, k_z, \omega) = [\tilde{u}, \tilde{v}, \tilde{w}]^T$ ,  $\mathbf{U} = [U, V, W]^T$ ,  $\tilde{\mathbf{f}}(k_x, k_z, \omega) = [\tilde{f}_u, \tilde{f}_v, \tilde{f}_w]^T$  denotes the nonlinear advection terms and  $\tilde{p}(k_x, k_z, \omega)$  is the pressure, all of which are functions of wall-normal distance  $y$ . The operators  $\hat{\nabla} = [ik_x, \partial_y, ik_z]^T$  and  $\hat{\Delta} = \partial_{yy} - k_x^2 - k_z^2$ . Here, the triplet  $(k_x, k_z, \omega)$  denotes the streamwise and spanwise wavenumbers and the temporal frequency, respectively. The length, velocity and time scales are non-dimensionalised using  $\delta$ ,  $u_\tau$  and  $\delta/u_\tau$ , respectively, and  $k_x$ ,  $k_z$  and  $\omega$  are non-dimensionalised using  $\delta^{-1}$ ,  $\delta^{-1}$  and  $u_\tau/\delta$ , respectively. Further, to facilitate the notation, we define  $k_x^\circ = 2\pi\delta k_x/L_x$  and  $k_z^\circ = 2\pi\delta k_z/L_z$  such that integer values of  $k_x^\circ$  and  $k_z^\circ$  indicate the number of wavelengths that fit in the streamwise and spanwise domain of size  $(L_x, L_z)$ , and, for any function  $\zeta(k_x, k_z, \omega)$ ,  $\zeta^{(a,b,c)} = \zeta(k_x^\circ = a, k_z^\circ = b, \omega = c)$ .

Equivalently, we can express the Navier–Stokes equations for  $(k_x, k_z, \omega) \neq (0, 0, 0)$  as

$$\begin{bmatrix} \tilde{\mathbf{u}}(k_x, k_z, \omega) \\ \tilde{p}(k_x, k_z, \omega) \end{bmatrix} = \mathcal{H}(k_x, k_z, \omega) \begin{bmatrix} \tilde{\mathbf{f}}(k_x, k_z, \omega) \\ 0 \end{bmatrix}. \quad (2.2)$$

We refer to the linear operator  $\mathcal{H}(k_x, k_z, \omega)$ , which takes  $\mathbf{U}$  as input, as the resolvent operator. The singular value decomposition of the resolvent operator returns an ordered basis pair  $\{\tilde{\boldsymbol{\psi}}_j, \tilde{\boldsymbol{\phi}}_j\}$  along with the associated singular value  $\sigma_j$  ( $\sigma_1 \geq \sigma_2 \geq \dots \geq 0$ ), which can be used to express (2.2) as

$$\begin{bmatrix} \tilde{\mathbf{u}}(k_x, k_z, \omega) \\ \tilde{p}(k_x, k_z, \omega) \end{bmatrix} = \sum_{j=1}^{\infty} \sigma_j(k_x, k_z, \omega) \tilde{\boldsymbol{\psi}}_j(k_x, k_z, \omega) \left\langle \tilde{\boldsymbol{\phi}}_j(k_x, k_z, \omega), \begin{bmatrix} \tilde{\mathbf{f}}(k_x, k_z, \omega) \\ 0 \end{bmatrix} \right\rangle, \quad (2.3)$$

where  $\langle \cdot, \cdot \rangle$  is the inner product corresponding to the kinetic energy norm, and the basis vectors  $\tilde{\boldsymbol{\phi}}_i$  and  $\tilde{\boldsymbol{\psi}}_i$  vectors are unitary. We refer to  $\tilde{\boldsymbol{\psi}}_j$  as the response modes and  $\tilde{\boldsymbol{\phi}}_j$  as the forcing modes. The former identifies the most amplified coherent structures, which are considered to contain most of the energy. The latter are the basis for the nonlinear terms that create the response modes via the linear resolvent operator.

While the eddy viscosity formulation of the resolvent analysis, as in Morra *et al.* (2019), has been shown to improve the prediction of statistics for most energetic streamwise-constant streaks, a more recent study by Symon, Illingworth & Marusic (2020) shows that eddy viscosity does not respect the conservative nature of the nonlinear energy transfer, which must sum to zero over all scales. Consequently, it is less effective for scales that receive energy from the nonlinear terms. Thus, for the purposes of this study, we find the original resolvent formulation without the additional eddy viscosity term more relevant.

Note that, due to the symmetry in the channel flow, the resolvent modes appear in pairs, and the modes corresponding to the two largest singular values,  $\sigma_1$  and  $\sigma_2$ , can be decomposed into two components that are symmetric about  $y = 1$ . For the purpose of identifying modes that act primarily on the top or bottom of the channel, we define the principal mode as the linear combination of the two largest resolvent modes as follows. To find a principal forcing mode that acts mostly on the bottom half of the channel ( $0 \leq y \leq 1$ ), we first define the symmetric and antisymmetric modes as a linear combination that is symmetric or antisymmetric, respectively, with respect to  $y = 1$  and has positive real component when integrated from  $y = 0$  to  $y = 1$ . We then focus on the principal forcing mode  $\tilde{\boldsymbol{\phi}}_1 = [\tilde{\phi}_{1,u}, \tilde{\phi}_{1,v}, \tilde{\phi}_{1,w}, 0]^T$  computed by taking the sum of the symmetric and antisymmetric linear combination of the pair, such that the sum of the



two will mostly affect flow in the bottom half ( $0 \leq y \leq 1$ ) of the channel. Consequently,  $\tilde{\phi}_2$  is the difference of the symmetric and antisymmetric linear combination of the pair corresponding to these two largest singular values such that the projection of the resolvent mode will mostly affect flow in the top half of the channel. All subsequent modes  $\tilde{\phi}_{3,4,\dots}$  are defined analogously.

## 2.2. Numerical simulation

Two sets of numerical simulations are performed by solving the incompressible Navier–Stokes equations

$$\frac{\partial \bar{\mathbf{U}}}{\partial t} = -(\bar{\mathbf{U}} \cdot \nabla) \bar{\mathbf{U}} - \nabla p + \frac{1}{Re_\tau} \Delta \bar{\mathbf{U}}, \quad \nabla \cdot \bar{\mathbf{U}} = 0, \quad (2.4a,b)$$

using a computational domain tailored to isolate the most energetic eddies in either the buffer layer (Jiménez & Moin 1991) or the log layer (Bae & Lozano-Durán 2019). This can be considered the simplest numerical set-up to study the SSP for wall-bounded energy-containing eddies of a given size.

In order to isolate the most energetic eddies in the buffer layer, defined as  $5 < y^+ < 30$ , where the superscript  $+$  denotes viscous units, we perform a direct numerical simulation (DNS) of an incompressible turbulent channel flow at  $Re_\tau \approx 186$ . The simulations are performed by discretising the incompressible Navier–Stokes equations with a staggered, second-order-accurate, central finite-difference method in space (Orlandi 2000), and an explicit third-order-accurate Runge–Kutta method for time advancement (Wray 1990). The system of equations is solved via an operator splitting approach (Chorin 1968). Periodic boundary conditions are imposed in the streamwise and spanwise directions, and the no-slip condition is applied at the walls. The code has been validated in previous studies of turbulent channel flows (Bae *et al.* 2018, 2019). The streamwise, wall-normal and spanwise domain sizes are  $L_x^+ \approx 340$ ,  $L_y^+ \approx 372$  and  $L_z^+ \approx 170$ , respectively. Jiménez & Moin (1991) showed that simulations in this domain constitute an elemental structural unit containing a single streamwise streak and a pair of staggered quasi-streamwise vortices, which reproduce reasonably well the statistics of the flow in larger domains. The grid spacings in the streamwise and spanwise directions are uniform, with  $\Delta_x^+ \approx 10.6$  and  $\Delta_z^+ \approx 5.3$ ; non-uniform meshes are used in the wall-normal direction, with the grid stretched towards the wall according to a hyperbolic tangent distribution with  $\min(\Delta_y^+) \approx 0.17$  and  $\max(\Delta_y^+) \approx 7.6$ .

In the case of the log layer, defined as  $3Re_\tau^{-1/2} < y < 0.15$  (Marusic *et al.* 2013), we perform a large-eddy simulation (LES) of an incompressible turbulent channel flow at  $Re_\tau \approx 2003$  with modified wall boundary conditions. The set-up of the simulations is similar to the buffer-layer case, but the no-slip boundary condition at the walls is replaced by a slip boundary condition of the form

$$\bar{\mathbf{U}} = l_s \frac{\partial \bar{\mathbf{U}}}{\partial y}, \quad \bar{\mathbf{V}} = l_s \frac{\partial \bar{\mathbf{V}}}{\partial y}, \quad \bar{\mathbf{W}} = l_s \frac{\partial \bar{\mathbf{W}}}{\partial y}, \quad (2.5a-c)$$

where  $l_s = 0.05$  is the slip length. The choice to use LES with the slip boundary condition rather than DNS is deliberate in order to remove the presence of small-scale motions from the flow (Leonard 1975; Hwang & Bengana 2016; Cossu & Hwang 2017; Bae & Lozano-Durán 2019) and to suppress the formation of near-wall viscous layers and buffer-layer eddies (Lozano-Durán & Bae 2016, 2019a; Bae & Lozano-Durán 2019), as

we are interested in energy-containing motions of the log layer. This modified channel flow is tailored to isolate the large-scale motions of the log layer. While the simulated log layer produces healthy turbulence only in a limited range of wall-normal locations, this allows a simplified approach to study the SSP of the isolated scales.

The choice of the slip length is such that the adaptation length (Lozano-Durán & Bae 2019a), i.e. the vertical distance from the boundary above which the flow recovers to the nominal no-slip flow statistics, is below the lower bound of the log layer for this Reynolds number. The anisotropic minimum dissipation model (Rozema *et al.* 2015) is used as the subgrid-scale model for the LES. The streamwise, wall-normal and spanwise domain sizes of the simulation are  $L_x \approx 1.57$ ,  $L_y = 2$  and  $L_z \approx 0.79$ , respectively. This domain size corresponds to a minimal box simulation for the log layer and is sufficient to isolate the relevant dynamical structures involved in the bursting process (Flores & Jiménez 2010). Moreover, the choice of the domain size is such that the wall-normal distance below which flow exhibits healthy turbulence,  $l_d \approx L_z/3 \approx 0.25$  (Flores & Jiménez 2010), is above the upper bound of the log layer. The domain is discretised using  $N_x = 256$  and  $N_z = 64$  points in the streamwise and spanwise directions, and  $N_y = 101$  in the wall-normal direction. The grid spacings in the streamwise and spanwise directions are uniform with  $\Delta_x \approx 0.006$  and  $\Delta_z \approx 0.012$  such that the grid captures 90 % of the turbulent kinetic energy at  $y = 0.15$ , which is necessary to accurately capture the coherent structures present in the flow (Lozano-Durán & Bae 2019b). Non-uniform meshes are used in the wall-normal direction, with the grid stretched towards the wall according to a hyperbolic tangent distribution with  $\min(\Delta_y) \approx 0.003$  and  $\max(\Delta_y) \approx 0.04$ . Bae & Lozano-Durán (2019) showed that simulations in this domain with the modified boundary conditions reproduce the statistics in the log layer of the flow in larger domains while suppressing the formation of the near-wall eddies. For details regarding this simulation, the reader is referred to Bae & Lozano-Durán (2019).

The flow is simulated for more than 100 time units after transients for computation of the mean streamwise velocity profile in the undisturbed minimal channel, which we label  $U^F$ , shown in figure 1(a,b) for the two cases. The resolvent modes  $\tilde{\phi}_i$  and  $\tilde{\psi}_i$  for the minimal buffer and log layer were then computed with the respective  $U^F$ , using the same staggered, second-order-accurate, central finite-difference method in the wall-normal direction and the corresponding wall boundary conditions. The Fourier discretisation in the computation of the resolvent modes in the streamwise and spanwise directions was updated to use the modified wavenumber corresponding to a staggered second-order finite-difference method. The mismatch of the mean velocity profile for the buffer-layer case away from the wall ( $y^+ > 30$ ) is expected due to the smaller box, which is designed to remove larger scales of motion and is in agreement with previous studies utilising minimal channels (Jiménez & Moin 1991). In the log-layer case, the simulation is designed to remove both the viscous scales and subgrid scales as well as the larger outer-region scales, resulting in the mismatch in both the buffer and the outer region. The disruption of the viscous scale can be better observed from the lack of the inner peak in the streamwise turbulence intensity (figure 1d).

The new simulations are started from an initial condition from the channel flow described above that is modified such that  $\bar{u} = U^F$ . Then, an appropriate forcing at each time step is applied to (2.4a) to freeze the mean such that  $\bar{u} = U^F$ , or equivalently  $\partial \bar{u} / \partial t = 0$ . This is done by setting the  $(k_x, k_z) = (0, 0)$  mode of the right-hand side of (2.4a) to zero at each time step. The mean velocity profile is frozen so that the most amplified resolvent modes remain constant throughout the simulation. It is also consistent with the aim of the study, which is to characterise the mechanisms that sustain the

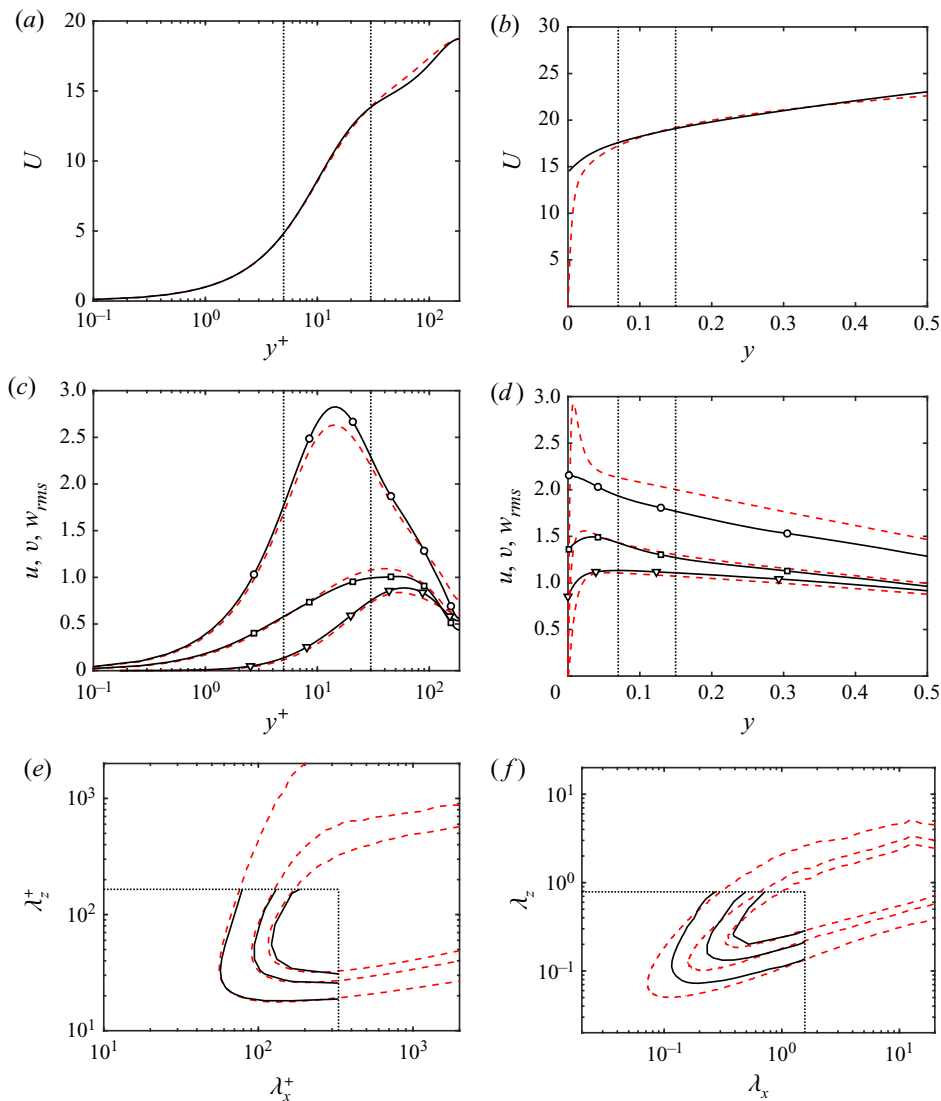


Figure 1. (a) Mean streamwise velocity profile, (c) turbulence intensities and (e) energy spectra at  $y^+ = 15$  of the buffer-layer minimal channel (black solid line) compared to the mean velocity profile of the channel flow for the domain size of  $12\pi \times 2 \times 4\pi$  (red dashed line) at  $Re_\tau \approx 186$  from Del Alamo & Jiménez (2003). (b) Mean streamwise velocity profile, (d) turbulence intensities and (f) energy spectra at  $y = 0.15$  of the log-layer minimal channel (black solid line) compared to the mean velocity profile of the channel flow for the domain size of  $8\pi \times 2 \times 3\pi$  (red dashed line) at  $Re_\tau \approx 2003$  from Hoyas & Jiménez (2006). The mean streamwise velocity profile for the minimal channel in (b) is vertically shifted by 8.4 wall units such that the velocity at  $y = 0.15$  coincides with the larger-domain case. Turbulence intensities are shown for streamwise ( $\circ$ ), wall-normal ( $\nabla$ ) and spanwise ( $\square$ ) components. Dotted lines in (a–d) indicate lower and upper domains for buffer and log layer for corresponding cases. Dotted lines in (e, f) indicate the domain size of the minimal channel. Contour levels are 1%, 5% and 10% for (e) and 10%, 25% and 40% for (f) of the maximum value of the large-domain cases.

fluctuating velocities generated by the actual turbulent mean flow. Tuerke & Jiménez (2013) showed that turbulent channel flows with prescribed correct mean velocity profiles result in naturally occurring fluctuating velocities. An additional case without freezing the



mean, i.e. not applying the additional forcing to set  $\partial \bar{u} / \partial t = 0$ , is performed later in § 3.1 to study the effect of freezing the mean.

The turbulence intensities and the energy spectra of the frozen-mean minimal-domain simulations are compared to the large-domain counterparts in figure 1(c–f). We see that, in the regions bounded by the vertical dotted lines in figure 1(c,d), which signify the lower and upper bounds of the buffer and log layer in the respective cases, the turbulence intensities follow the trend of its large-domain counterpart. The underprediction of the turbulence intensities in the log-layer simulation is due to the use of LES, where energy from the small- and largest-scale motions are not included. The two-dimensional premultiplied energy spectra at  $y^+ = 15$  and  $y = 0.15$ , respectively, are shown in figure 1(e,f), and the results match well with the large-domain counterparts, with the exception of the missing large-scale motions, which extend beyond the respective domains, and the small-scale contributions in the log layer, which are modelled and not resolved in LES.

In order to study the effect of the forcing modes on the flow, a separate simulation is advanced in time by removing the projection of the nonlinear term  $\mathbf{f}' = -(\mathbf{u}' \cdot \nabla) \mathbf{u}'$  onto the resolvent forcing mode  $\tilde{\boldsymbol{\phi}}_1$  for the chosen  $(k_x, k_z, \omega)$  at each time step. Note that  $\mathbf{u}' = \mathbf{u}$  in the case when the mean is frozen in time. This is done by first taking the Fourier transform of the nonlinear term in the homogeneous directions and computing the projection

$$\hat{\mathbf{g}}_1(k_x, k_z, \omega) = \left\langle \begin{bmatrix} \hat{\mathbf{f}}'(k_x, k_z) \\ 0 \end{bmatrix}, \tilde{\boldsymbol{\phi}}_1(k_x, k_z, \omega) \right\rangle \begin{bmatrix} \tilde{\boldsymbol{\phi}}_{1,u}(k_x, k_z, \omega) \\ \tilde{\boldsymbol{\phi}}_{1,v}(k_x, k_z, \omega) \\ \tilde{\boldsymbol{\phi}}_{1,w}(k_x, k_z, \omega) \end{bmatrix} \quad (2.6a,b)$$

at each time step. The projection is then removed by subtracting the inverse Fourier-transformed  $\hat{\mathbf{g}}_1$  from the right-hand side of (2.4a) and advancing in time. Symmetry of the Fourier modes is preserved by also removing  $\hat{\mathbf{g}}_1^{*\text{T}}$ , the conjugate of  $\hat{\mathbf{g}}_1$  (where superscript  $*$  denotes conjugate transpose and  $\text{T}$  denotes transpose), from the nonlinear term  $\hat{\mathbf{f}}'(-k_x, -k_z)$  at each time step. Projections onto  $\tilde{\boldsymbol{\phi}}_i$  are analogously defined as  $\hat{\mathbf{g}}_i$ .

For the remainder of the paper, we denote the channel flow simulation with the mean fixed at each time step but no forcing mode removed as the ‘undamped’ case and the simulation with the forcing mode removed as the ‘damped’ case.

### 3. Effect of principal forcing modes on turbulence intensities

#### 3.1. Buffer layer

As mentioned in the previous section, a choice of the target wavenumbers is required to identify the forcing modes that are removed at each time step. For this, we target the Fourier modes with the most energy content. Figure 2(a) shows the spectral energy content,  $\hat{E}(k_x, k_z) = \frac{1}{2}(\hat{\mathbf{u}}^* \hat{\mathbf{u}})$ , at  $y^+ \approx 15$  for the buffer-layer case, as a function of streamwise and spanwise wavenumbers. There is a clear peak at  $(k_x^\circ, k_z^\circ) = (0, \pm 1)$ . This is consistent with the fact that the domain size of the minimal channel is such that it isolates flow structures to be infinitely long in the streamwise direction and once-periodic in the spanwise direction. Thus, for our analysis, we choose the streamwise and spanwise wavenumbers  $(k_x^\circ, k_z^\circ) = (0, 1)$ . This choice of streamwise and spanwise wavenumbers also coincides with the  $(k_x, k_z)$  with the largest  $\sigma_1$  over all values of  $\omega$ , which shows not only that this wavenumber pair holds the most energy, but also that it has the

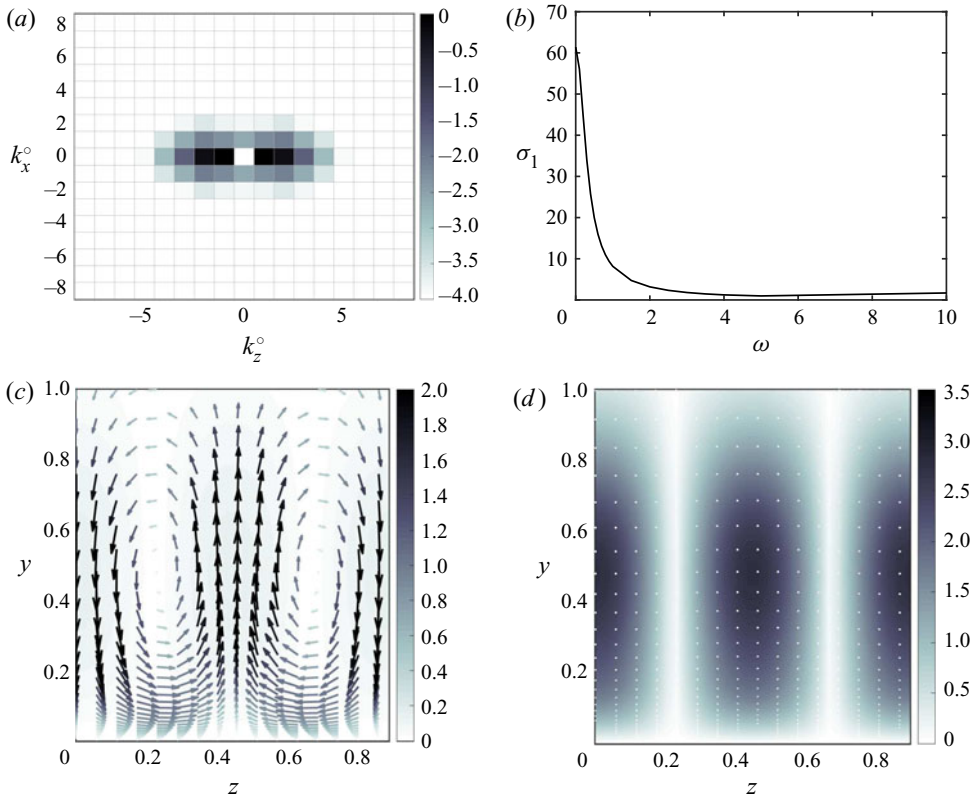


Figure 2. (a) Logarithm of spectral energy content,  $\log(\hat{E})$ , at  $y^+ \approx 15$  for the buffer-layer case. (b) Principal singular value  $\sigma_1$  as a function of  $\omega$  for  $(k_x^o, k_z^o) = (0, 1)$  for the buffer layer. (c,d) The  $y$ - $z$  plane of the principal (c) forcing mode  $\tilde{\phi}_1$  and (d) response mode for  $(k_x^o, k_z^o, \omega) = (0, 1, 0)$  for the buffer-layer case. The streamwise component (colour) and the cross-flow component (arrows) are given, with the colour bar indicating magnitude for both components.

highest amplification within the resolvent framework. The temporal frequency is given as  $\omega = 0$ , which corresponds to the highest  $\sigma_1$  for  $(k_x^o, k_z^o) = (0, 1)$  (figure 2b). Note that the projection (2.6a,b) includes the contributions from various temporal frequencies apart from  $\omega = 0$  due to the fact that (2.6a,b) is time-dependent. However, it ascertains the removal of this particular forcing mode. Also, the singular value associated with  $\omega = 0$  is much larger than other temporal frequencies, making the removal of other frequency contents relatively less significant.

The principal forcing and response modes for this particular frequency–wavenumber triplet are given in figure 2(c,d). The forcing mode highlights a pair of streamwise rolls in the nonlinear term, i.e. the Reynolds stress contribution to the advection term, spanning the entire channel half-height. A much weaker streamwise streak in the nonlinear term whose magnitude  $(|\tilde{\phi}_{1,u}|)$  is approximately 5 % of that of the streamwise rolls,  $(\tilde{\phi}_{1,v}^2 + \tilde{\phi}_{1,w}^2)^{1/2}$ , is also present. The response modes exhibit streamwise streaks with alternating signs of the same magnitude (only the magnitude is shown in figure 2d) and weak cross-flow. The values above  $y = 1$  are negligible due to our definition of the principal mode. This shows that the streamwise rolls generated by the nonlinear term can be transformed through a linear process, i.e. the lift-up mechanism, to streamwise streaks, as expected from previous studies of the SSP. For the given  $(k_x, k_z, \omega)$ , the principal forcing mode contains the largest

energetic contribution under unit broadband forcing (approximately 85 %), defined as  $(\sigma_i^2 + \sigma_{i+1}^2) / \sum_{k=1}^{\infty} \sigma_k^2$  for each  $\phi_i$  for  $i = 1, 3, 5, \dots$ . The subsequent modes  $\phi_3$  and  $\phi_5$  have an energetic contribution of approximately 12 % and 2 %, respectively (see figure 5a). The large separation in the singular values indicates that the principal forcing mode will be amplified by almost an order of magnitude more than the other forcing modes and thus will be integral in the SSP.

The effect of removing  $\hat{g}_1^{(0,1,0)}$  can be seen in figure 3(a) in the form of the turbulence kinetic energy (TKE) evolution in time. Although not shown, the dissipation rate as a function of time exhibits similar trends to that of the TKE. Figure 3(a) shows that removing  $\hat{g}_1^{(0,1,0)}$  reduces the TKE significantly. The steady-state root-mean-square (r.m.s.) velocity fluctuation profiles for this case are given in figure 3(b). As expected, the effect of removing the principal forcing term is observed only on the bottom half of the channel where the principal forcing term was isolated, with only minor changes in the statistics in the top half of the channel. At any instant in time of the undamped case, the contribution of  $\hat{g}_1^{(0,1,0)}$  to the nonlinear advection term, defined as the average-in-time ratio of  $\int \hat{g}_1^{(0,1,0)*} \hat{g}_1^{(0,1,0)} dy$  to  $\iiint f'^2 dx dy dz$ , is less than 0.9 %, and removing the same magnitude randomly from the advection term at each time step had no effect on the one-point statistics, which supports the importance of the spatial structure of the mode being projected out to the turbulent flow. Furthermore, if we remove  $\frac{1}{2} \hat{g}_1^{(0,1,0)}$  at each time step rather than  $\hat{g}_1^{(0,1,0)}$ , the impact on the turbulence statistics is negligible compared to the undamped case, which further highlights the importance of the principal forcing term.

In the case where the mean flow is not frozen but rather is allowed to evolve in time (figure 4a), the time evolution of TKE follows similar results as shown in figure 3(a) until  $t \approx 12$ , where it starts to increase again. This is due to the change in the mean velocity profile, as shown in figure 4(b). The initial reduction of turbulence intensities changes the dynamics of the flow such that the mean velocity profile approaches the laminar profile on the bottom half of the channel. The drastic change in the mean profile invalidates the relevance of the principal forcing mode obtained from the turbulent mean state,  $U^F$ , and causes the TKE to increase again. Even after the TKE becomes statistically stationary,  $t > 20$ , the new equilibrium state after transients shown in figure 4(b) differs from the turbulence with mean profile  $U^F$ .

In order to study the effects of removing subsequent forcing modes, we repeat the previous frozen-mean experiment, but removing either  $\hat{g}_3^{(0,1,0)}$  or  $\hat{g}_5^{(0,1,0)}$ , the secondary and tertiary forcing modes restricted primarily to the bottom half of the channel as defined in § 2.1, instead of  $\hat{g}_1^{(0,1,0)}$ . We see that turbulence is sustained in both cases from figure 3(c), but the extreme peaks in TKE observed in the undamped case are not as prominent. We can also see in figure 3(d) that, while the effect of removing  $\hat{g}_3^{(0,1,0)}$  still has some impact on the steady-state turbulence intensities, especially around  $y^+ \approx 15$ , the net change in the statistics is much smaller than that of removing  $\hat{g}_1^{(0,1,0)}$ . Removing  $\hat{g}_5^{(0,1,0)}$  has no impact on one-point statistics, and similar results are expected of subsequent forcing modes. Additionally, removing  $\hat{g}_3^{(0,1,0)}$  or  $\hat{g}_5^{(0,1,0)}$  in conjunction with  $\hat{g}_1^{(0,1,0)}$  (not shown) resulted in similar statistics as removing only  $\hat{g}_1^{(0,1,0)}$ . At any instant in time, the average contribution of  $\hat{g}_3^{(0,1,0)}$  or  $\hat{g}_5^{(0,1,0)}$  in the undamped case is statistically similar to the contribution of  $\hat{g}_1^{(0,1,0)}$  at 0.9 % of the total advection term, which shows the dominant impact of the principal forcing mode on the SSP.

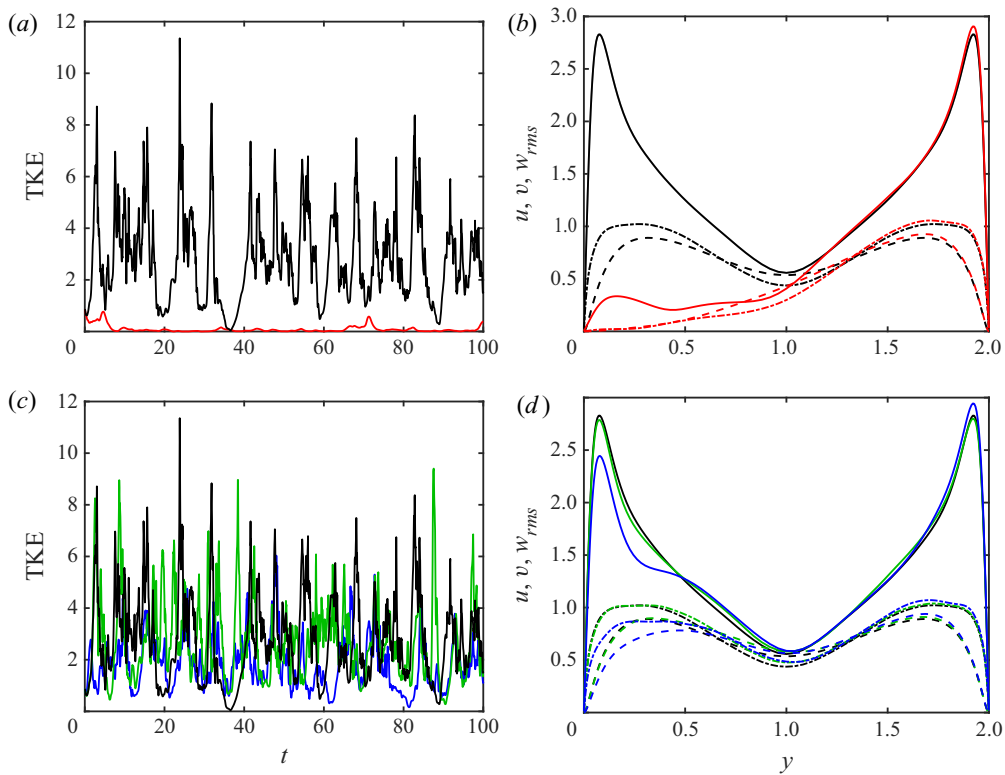


Figure 3. (a) Temporal evolution of TKE at  $y^+ \approx 15$  for the damped buffer-layer case removing  $\hat{g}_1^{(0,1,0)}$  (red) and the undamped buffer-layer minimal channel (black). (b) Streamwise (solid line), wall-normal (dashed line) and spanwise (dash-dotted line) r.m.s. velocity fluctuations for the damped case removing  $\hat{g}_1^{(0,1,0)}$  (red) and the undamped (black) buffer-layer minimal channel. (c,d) Same as (a,b), but removing  $\hat{g}_3^{(0,1,0)}$  (blue) or  $\hat{g}_5^{(0,1,0)}$  (green) at each time step instead of  $\hat{g}_1^{(0,1,0)}$ .

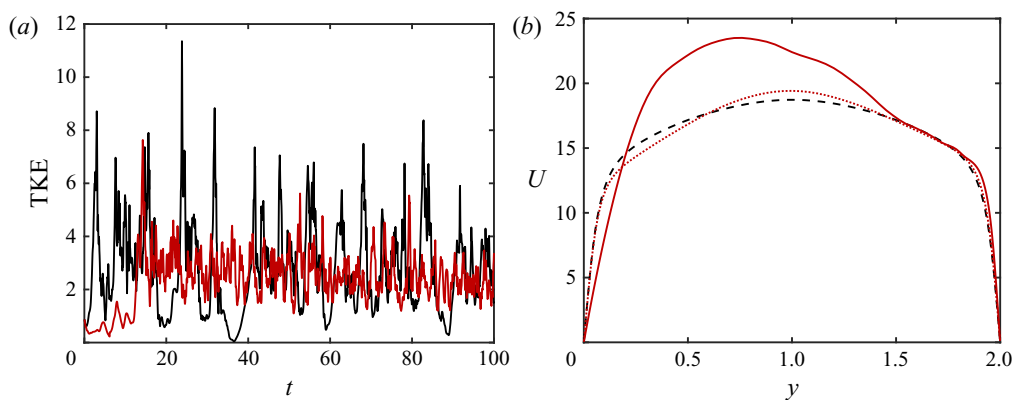


Figure 4. (a) Temporal evolution of TKE at  $y^+ \approx 15$  for the damped buffer-layer case removing  $\hat{g}_1^{(0,1,0)}$  without fixing the mean (maroon) and the undamped buffer-layer minimal channel (black). (b) Mean streamwise velocity corresponding to  $t = 12$  (maroon solid line) and averaged over  $20 < t < 100$  (maroon dotted line) for the case without fixing the mean and the fixed mean profile (black dashed line).

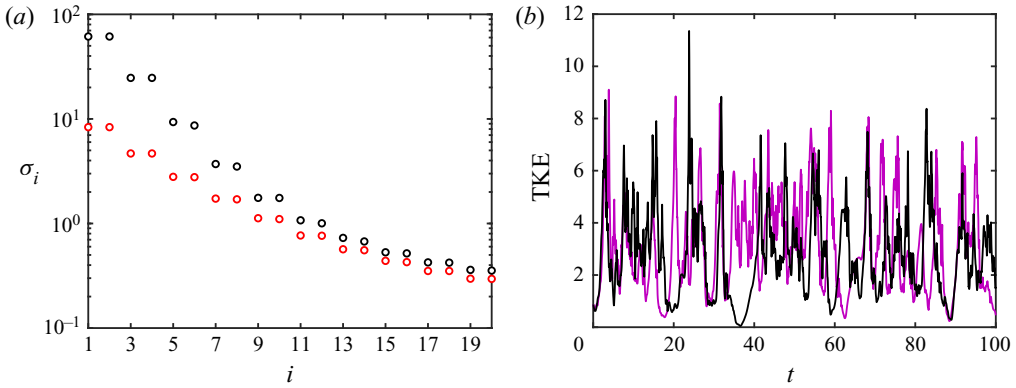


Figure 5. (a) Amplification factors  $\sigma_i$  for  $(k_x^\circ, k_z^\circ, \omega) = (0, 1, 0)$  (black) and  $(k_x^\circ, k_z^\circ, \omega) = (0, 2, 0)$  (red) for the buffer-layer case. (b) Temporal evolution of TKE at  $y^+ \approx 15$  for the damped buffer-layer case removing  $\hat{g}_1^{(0,2,0)}$  (magenta) and the undamped buffer-layer minimal channel (black).

Additionally, we also repeat the experiment, removing  $\hat{g}_1^{(0,2,0)}$ , as  $(k_x^\circ, k_z^\circ) = (0, 2)$  contains a significant amount of energy in figure 2(a). However, compared to the triplet  $(k_x^\circ, k_z^\circ, \omega) = (0, 1, 0)$ , the amplification factor  $\sigma_1$  for  $(k_x^\circ, k_z^\circ, \omega) = (0, 2, 0)$  is an order of magnitude lower as seen in figure 5(a) and the principal mode has an energetic contribution of approximately 65 %, which is much lower than the 85 % for  $(k_x^\circ, k_z^\circ, \omega) = (0, 1, 0)$ . The resulting time evolution of TKE shown in figure 5(b) is hence much less affected than removing  $\hat{g}_1^{(0,1,0)}$ , and removing  $\hat{g}_1^{(0,2,0)}$  in conjunction with  $\hat{g}_1^{(0,1,0)}$  (not shown) resulted in marginal difference compared to removing only  $\hat{g}_1^{(0,1,0)}$ . Overall, the removal of the principal forcing mode corresponding to  $(k_x^\circ, k_z^\circ, \omega) = (0, 1, 0)$  has the most impact on the flow, as expected.

### 3.2. Logarithmic layer

Using the same approach as in the buffer-layer case, we identify the target wavenumbers for the log-layer case. Figure 6(a) shows  $\hat{E}(k_x, k_z) = \frac{1}{2}(\hat{\mathbf{u}}^* \hat{\mathbf{u}})$  at  $y \approx 0.15$  for the log-layer case, as a function of streamwise and spanwise wavenumbers. Again, there is a clear peak at  $(k_x^\circ, k_z^\circ) = (0, \pm 1)$ , which is consistent with the fact that the domain size of the minimal channel for the log layer is such that the most dominant flow structures are infinitely long in the streamwise direction and once-periodic in the spanwise direction. Thus, for our analysis, we again choose the streamwise and spanwise wavenumbers  $(k_x^\circ, k_z^\circ) = (0, 1)$ . However, note that, unlike in the buffer-layer case, the spectral energy content of the log-layer case is distributed among various combinations of  $k_x$  and  $k_z$ , in particular with large contributions from  $(k_x^\circ, k_z^\circ) = (\pm 1, \pm 1)$ , indicating a more complex phenomenon in the SSP that cannot be isolated to one wavenumber, as seen in figure 6(a). However, similar to the analysis on  $(k_x^\circ, k_z^\circ) = (0, 2)$  for the buffer-layer case, the largest singular values as well as the spectral gap for the non-fundamental wavenumbers are significantly lower than that of  $(k_x^\circ, k_z^\circ) = (0, 1)$ , indicating that the effect of the principal resolvent modes for  $(k_x^\circ, k_z^\circ) \neq (0, 1)$  are not as dominant as that of  $(k_x^\circ, k_z^\circ) = (0, 1)$ . The temporal frequency identified by the highest  $\sigma_1$  for  $(k_x^\circ, k_z^\circ) = (0, 1)$  (figure 6b) is  $\omega = 0$ , but the values of  $\sigma_1$  do not decay as fast as in the buffer-layer case, indicating that more combinations of  $\omega$  may be involved compared to the buffer-layer case.



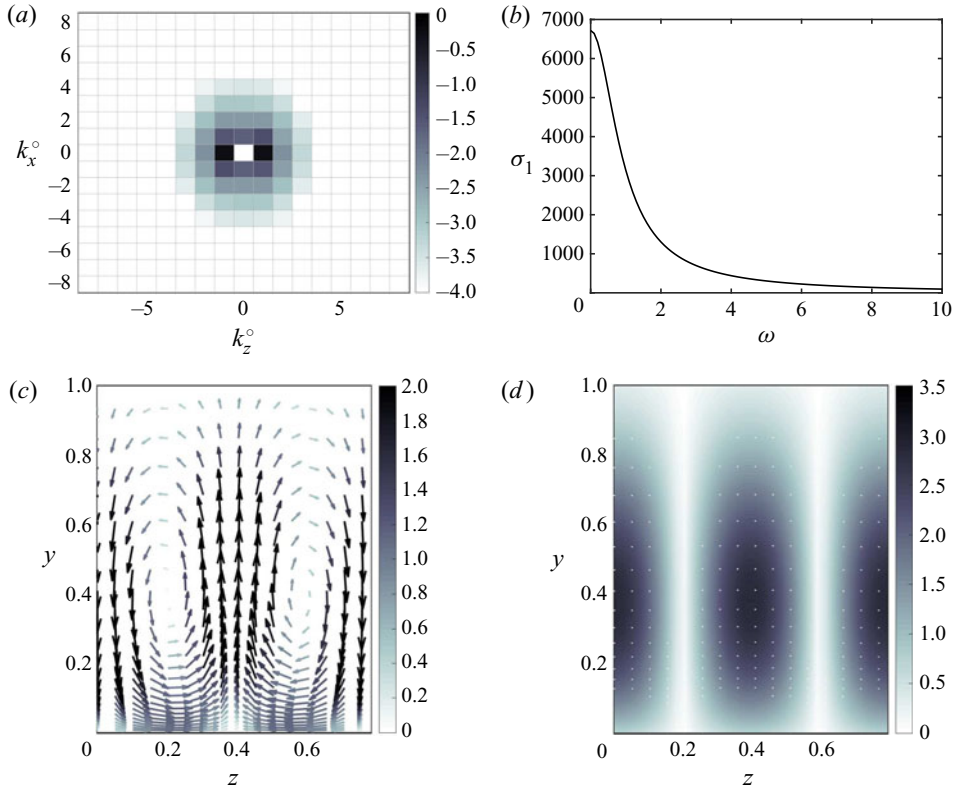


Figure 6. (a) Logarithm of spectral energy content,  $\log(\hat{E})$ , at  $y \approx 0.15$  for the log-layer case. (b) Principal singular value  $\sigma_1$  as a function of  $\omega$  for  $(k_x^o, k_z^o) = (0, 1)$  for the log-layer case. (c,d) The  $y$ - $z$  plane of the principal (c) forcing mode  $\tilde{\phi}_1$  and (d) response mode for  $(k_x^o, k_z^o, \omega) = (0, 1, 0)$  for the log-layer case. The streamwise component (colour) and the cross-flow component (arrows) are given, with the colour bar indicating magnitude for both components.

The principal forcing and response modes for this particular frequency–wavenumber triplet are given in figure 6(c,d). Despite the different Reynolds number and the wall boundary condition, the forcing and response modes of the log layer are similar to those of the buffer layer. The forcing mode highlights a pair of streamwise rolls spanning the entire channel half-height, and the response modes exhibit streamwise streaks with alternating signs of the same magnitude. For the given  $(k_x, k_z, \omega)$ , the principal forcing mode contains the largest energetic contribution under unit broadband forcing (approximately 81 %), similar to the buffer-layer case. The similarity in the identified principal resolvent modes indicates the similarity in the underlying mechanism for the SSP of the buffer and log layers, as has been hypothesised in the literature.

The fact that the log-layer structure of the minimal flow unit spans the full boundary layer thickness can be further explained by the self-similar attached-eddy hypothesis (Townsend 1976; Perry & Chong 1982; Meneveau & Marusic 2013; Agostini & Leschziner 2017; Marusic & Monty 2019). McKeon (2019) has recently identified that an isolated resolvent mode with a given convection velocity constitutes only part of the full attached eddy, and a geometric progression of such modes needs to be considered for the fair comparison to the attached eddies. In particular, a single wall-normal location of the log layer will be affected by a series of wall-attached eddies whose footprint includes the

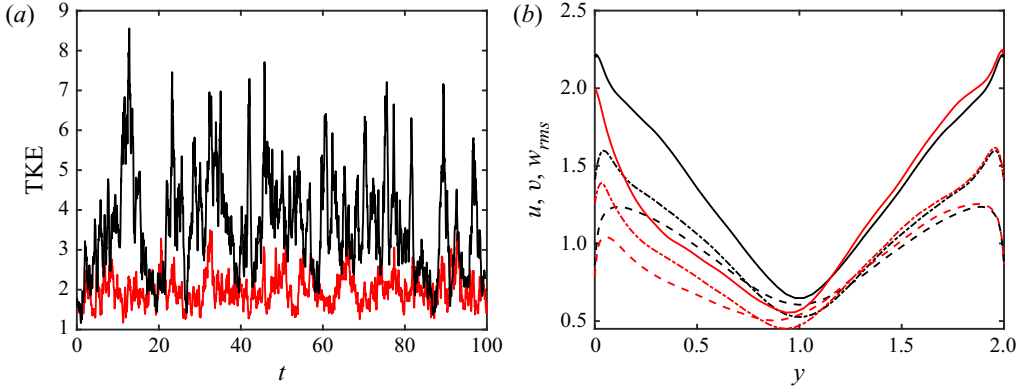


Figure 7. (a) Temporal evolution of TKE at  $y \approx 0.15$  for the damped log-layer case removing  $\hat{g}_1^{(0,1,0)}$  (red) and the undamped log-layer minimal channel (black). (b) Streamwise (solid line), wall-normal (dashed line) and spanwise (dash-dotted line) r.m.s. velocity fluctuations for the damped log-layer case removing  $\hat{g}_1^{(0,1,0)}$  (red) and the undamped (black) log-layer minimal channel.

given wall-normal height. From this viewpoint, the structures that impact the log layer would span the whole half-channel as observed in the current case.

The results of removing  $\hat{g}_1^{(0,1,0)}$  for the log layer are shown in figure 7. The TKE does not reduce as significantly as in the buffer-layer case, as seen in the time evolution of TKE in figure 7(a) and the time-averaged turbulence intensities in figure 7(b); however, we do see a significant reduction in the TKE. Similar to the buffer-layer case, the dissipation rate (not shown) follow the trends of the TKE. The relatively smaller effect of the principal forcing modes in the log layer is due to the complexity and the disorganisation of the log layer itself. Unlike the buffer layer, where only one scale is isolated by the minimal domain, the log layer still includes contributions from various scales that exist in the log layer (figure 6a), which makes it harder to affect the full system by removing only one scale. However, the significant reduction in TKE and turbulence intensities obtained by removing the principal forcing mode, which exhibit similar characteristics in both the buffer and log layer, shows that the mechanism in which turbulence self-sustains is similar in both regions. The results of removing secondary forcing modes and principal forcing modes for a different  $(k_x, k_z, \omega)$ , while not reported here, show comparable trends as seen in the buffer layer, where the impact on the flow statistics is marginal compared to that of  $\hat{g}_1^{(0,1,0)}$ .

#### 4. Nonlinear interaction

As demonstrated in the previous section, the principal forcing mode  $\tilde{\phi}_1^{(0,1,0)}$  identifies the most amplified nonlinear interaction for the most energetic wavenumber and is integral in sustaining turbulence in the near-wall cycle for both the buffer and log layers. In order to study the nonlinear interactions that produce this term through dyadic interactions, we decompose the nonlinear term as a convolution sum in Fourier space,

$$\hat{f}(k_x, k_z) = \sum_{k'_x, k'_z = -\infty}^{\infty} (\hat{u}(k'_x, k'_z) \cdot \hat{\nabla}) \hat{u}(k_x - k'_x, k_z - k'_z), \quad (4.1)$$

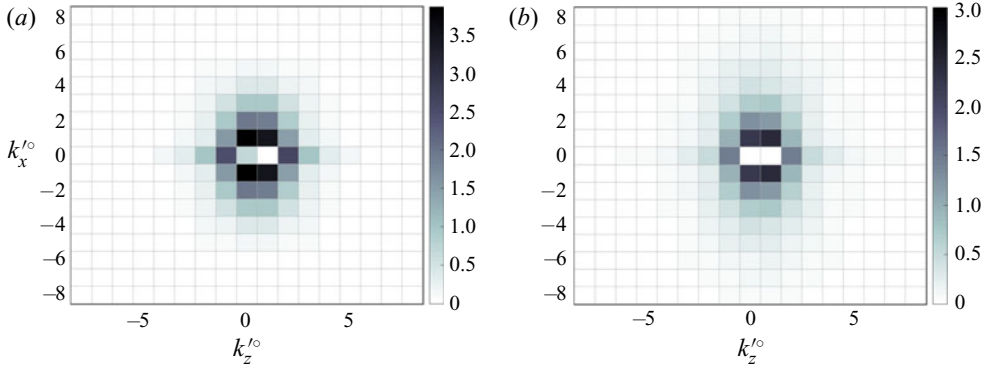


Figure 8. Average contribution of each convolution sum  $|\Pi(k'_x = 1, k'_z = 0; k_x = 0, k_z = 1, \omega = 0)|$  normalised by the total contribution  $|\sum_{k'_x, k'_z} \Pi(k'_x, k'_z; k_x = 0, k_z = 1, \omega = 0)|$  for the (a) buffer-layer case and (b) log-layer case.

which is a function of  $y$  and  $t$ . The contribution of each component of the convolution sum towards the projection of the principal forcing term onto  $\tilde{\phi}_1^{(0,1,0)}$  for any given flow field can be measured as

$$\Pi(k'_x, k'_z; k_x, k_z, \omega) = \left\langle \left[ \frac{(\hat{\mathbf{u}}(k'_x, k'_z) \cdot \hat{\mathbf{V}}) \hat{\mathbf{u}}(k_x - k'_x, k_z - k'_z)}{0}, \tilde{\phi}_1(k_x, k_z, \omega) \right] \right\rangle. \quad (4.2)$$

Note that integration over all  $k'_x$  and  $k'_z$  of  $\Pi(k'_x, k'_z)^{(0,1,0)}$  gives the projection coefficient computed in (2.6a,b), where, by abuse of notation, we define  $\Pi(k'_x, k'_z)^{(a,b,c)} = \Pi(k'_x, k'_z; k_x = a, k_z = b, \omega = c)$  and  $\Pi^{(a,b;c,d,e)} = \Pi(k'_x = a, k'_z = b; k_x = c, k_z = d, \omega = e)$ . Also, due to incompressibility,  $\Pi$  is symmetric with respect to  $(k_x, k_z)$  for each flow field; that is,  $\Pi(k'_x, k'_z; k_x, k_z, \omega) = \Pi(k_x - k'_x, k_z - k'_z; k_x, k_z, \omega)$ . The average spectral map of  $|\Pi(k'_x, k'_z)^{(0,1,0)}|$  normalised by the total contribution  $|\sum_{k'_x, k'_z} \Pi(k'_x, k'_z)^{(0,1,0)}|$  is computed from flow fields of the undamped minimal channel of the buffer and log layer and is depicted in figure 8. Both spectral maps show quantitatively similar features and identify two main sources of contribution from the wavenumber pair  $(k'_x, k'_z) = (1, 0)$  and  $((k_x - k'_x), (k_z - k'_z)) = (-1, 1)$  and its mirror image in the  $xy$ -plane,  $(k'_x, k'_z) = (-1, 1)$  and  $(-k'_x, 1 - k'_z) = (1, 0)$ , which account for approximately 40 % of the total contribution. This is consistent with the results from Hamilton *et al.* (1995), which used vorticity as a measure rather than the contribution towards resolvent forcing modes. While the contributions from other wavenumber pairs are not negligible, for the remainder of this paper, we focus on the two pairs of wavenumbers to identify the coherent structures responsible for the nonlinear forcing term and without loss of generality choose the pair  $(k'_x, k'_z) = (1, 0)$  and  $((k_x - k'_x), (k_z - k'_z)) = (-1, 1)$ .

To identify instantaneous flow configurations where the contribution towards  $\tilde{\phi}_1^{(0,1,0)}$  is strong or weak, we first observe values of  $\bar{\Pi}^{(1,0;0,1,0)} = |\Pi^{(1,0;0,1,0)}| / \langle \hat{\mathbf{f}}(k'_x = 1, k'_z = 0), \hat{\mathbf{f}}(k'_x = 1, k'_z = 0) \rangle^{1/2}$ , which represents the normalised contribution to the principal forcing term with respect to the total energy of the nonlinear term in the  $(k'_x, k'_z)$  mode, computed from flow fields of the undamped channel. We then determine the mean  $\mu$  and standard deviation  $\varsigma$  of the distribution of  $\bar{\Pi}^{(1,0;0,1,0)}$  over all time instants. The high-forcing-intensity events are defined as those with  $\bar{\Pi}^{(1,0;0,1,0)} > \mu + 2\varsigma$  and

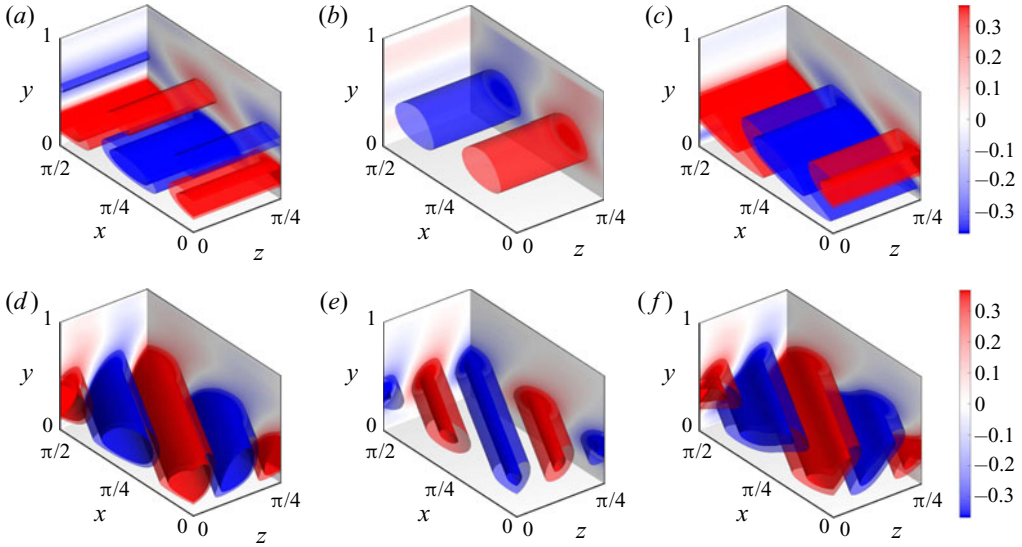


Figure 9. Average (a,d)  $\mathcal{F}^{-1}(\hat{u})$ , (b,e)  $\mathcal{F}^{-1}(\hat{v})$  and (c,f)  $\mathcal{F}^{-1}(\hat{w})$  for  $(k_x^o, k_z^o) = (1, 0)$  (a–c) and  $(-1, 1)$  (d–f) conditioned to high-forcing-intensity events for the buffer-layer case. The isosurfaces are 0.41 (solid red), 0.26 (transparent red),  $-0.26$  (transparent blue) and  $-0.41$  (solid blue).

low forcing-intensity events as those with  $\bar{\Pi}^{(1,0;0,1,0)} < \mu - 2\zeta$ . Both cases consist of approximately 5 % of the total events.

The average  $\mathcal{F}^{-1}(\hat{u}(k_x^o = 1, k_z^o = 0))$  and  $\mathcal{F}^{-1}(\hat{u}(k_x^o = -1, k_z^o = 1))$  conditioned to high-forcing-intensity events for the buffer layer are shown in figure 9, where  $\mathcal{F}^{-1}$  is the inverse Fourier transform. The modes are phase-shifted before averaging such that they are phase-aligned for the streamwise velocity component at  $y^+ \approx 40$  in an effort to centre the underlying structures at a fixed location. The coherent structures identified by the  $(k_x^o, k_z^o) = (1, 0)$  mode (figure 9a–c) are in the form of a pair of spanwise rolls that is being sheared in the spanwise direction by  $w$ . That is, the relative phase of the velocity components depicts the vertically displaced pairs of positive and negative streamwise velocity components located between the horizontally displaced pairs of positive and negative wall-normal velocity, forming a structure in the shape of a spanwise roll, which then are affected by the alternating sign of the  $w$  components. The  $(k_x^o, k_z^o) = (-1, 1)$  mode (figure 9d–f) shows oblique streaks, which are the components of meandering streaks, with high-speed streaks moving towards the wall and low-speed streaks moving away from the wall, corresponding to sweeps and ejections. Furthermore, the spatial autocorrelation coefficients of the streamwise, wall-normal and spanwise velocity fluctuations, denoted  $C_{uu}$ ,  $C_{vv}$  and  $C_{ww}$ , respectively, are computed, where

$$C_{qq}(x - x', y, z - z') = \frac{\mathbb{E}[q(x, y, z)q(x', y', z') \mid \bar{\Pi}^{(1,0;0,1,0)} > \mu + 2\zeta]}{\mathbb{E}[q(x, y, z)q(x, y, z) \mid \bar{\Pi}^{(1,0;0,1,0)} > \mu + 2\zeta]} \quad (4.3)$$

is the correlation conditioned to high-forcing-intensity events at  $y^+ \approx 40$  for the buffer layer and  $y' \approx 0.2$  for the log layer. Here,  $q \in \{u, v, w\}$  and  $\mathbb{E}[\cdot]$  is the expectation, or alternatively the average quantity over homogeneous spatial directions and instants. The correlations for both cases, shown in figure 10, reveal structures very similar to those highlighted by the time-averaged  $\mathcal{F}^{-1}(\hat{u}(k_x^o = 1, k_z^o = 0))$  and  $\mathcal{F}^{-1}(\hat{u}(k_x^o = -1, k_z^o = 1))$

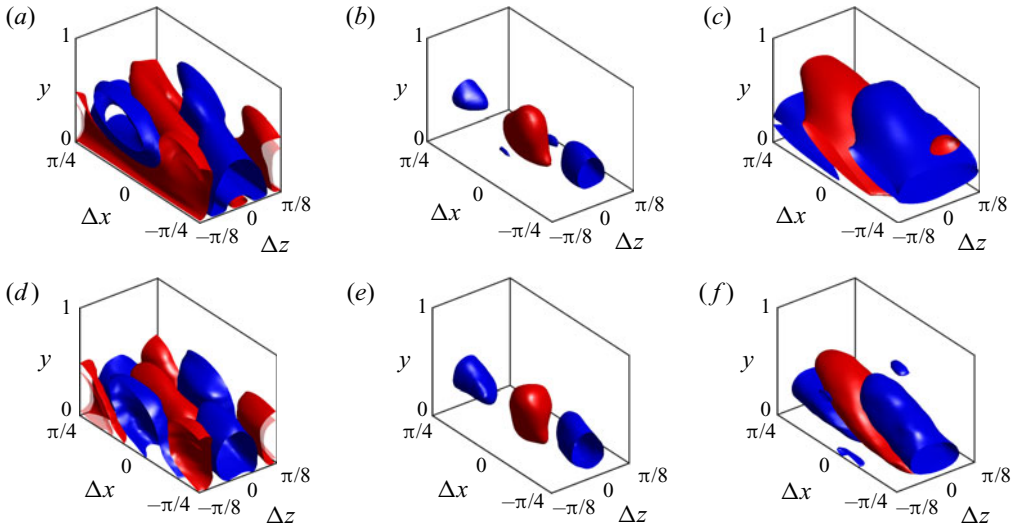


Figure 10. Correlations (a,d)  $C_{uu}$ , (b,e)  $C_{vv}$  and (c,f)  $C_{ww}$  conditioned to high-forcing-intensity events for the buffer layer (a–c) and log layer (d–f). The isosurfaces are 0.1 (red) and  $-0.04$  (blue).

and resemble spanwise-sheared spanwise rolls ( $C_{vv}$  and  $C_{ww}$ ) with oblique streaks ( $C_{uu}$ ), which are shared for both the buffer and log layer. This indicates that not only the linear mechanism but also the nonlinear mechanism driving the SSP are similar in both regions with similar structures forming the precursor events leading to strong intensities of the principal resolvent forcing term.

On the contrary, although not shown, average  $\mathcal{F}^{-1}(\hat{\mathbf{u}}(k_x^\circ = 1, k_z^\circ = 0))$  and  $\mathcal{F}^{-1}(\hat{\mathbf{u}}(k_x^\circ = -1, k_z^\circ = 1))$  conditioned to low-forcing-intensity events are less coherent for these wave parameters. This can be observed from the conditional correlation of the buffer-layer case in figure 11(a–c), where the streamwise and wall-normal velocities only show structures resembling straight streaks corresponding to wavenumbers  $(k_x^\circ, k_z^\circ) = (0, 2)$  and no structures resembling oblique streaks or spanwise rolls. Considering the fact that the total kinetic energy distributions for the strong and weak events are similar, these results show that the precursor to the nonlinear interaction that generates the principal forcing mode has more defined coherent structures in the form of spanwise rolls and oblique streaks, which interact to produce the principal forcing mode, which then plays an important role in the SSP of near-wall turbulence. Identifying these precursor events will allow development of new control mechanisms that aim to reduce the production of the resolvent forcing modes essential in sustaining turbulence.

Unlike the buffer-layer case, the streamwise correlation conditioned to low-forcing-intensity events shown in figure 11(d–f) is not as different from the high-forcing-intensity events for the log-layer case. The wall-normal correlation still shows clear positive and negative correlation pairs in the streamwise direction when conditioned to low-forcing-intensity events, and the spanwise correlations are less pronounced in the spanwise direction. The similarity in the streamwise component, although less pronounced in the low-forcing-intensity events, shows that, even if the principal forcing mode is removed, the flow will still self-sustain structures necessary for regenerating streamwise vortices, which is corroborated in § 3.2. However, the most significant difference in the correlations conditioned to strong- and weak-forcing-intensity events are the wall-normal components that partly form the spanwise rolls. These spanwise rolls are observed in cases



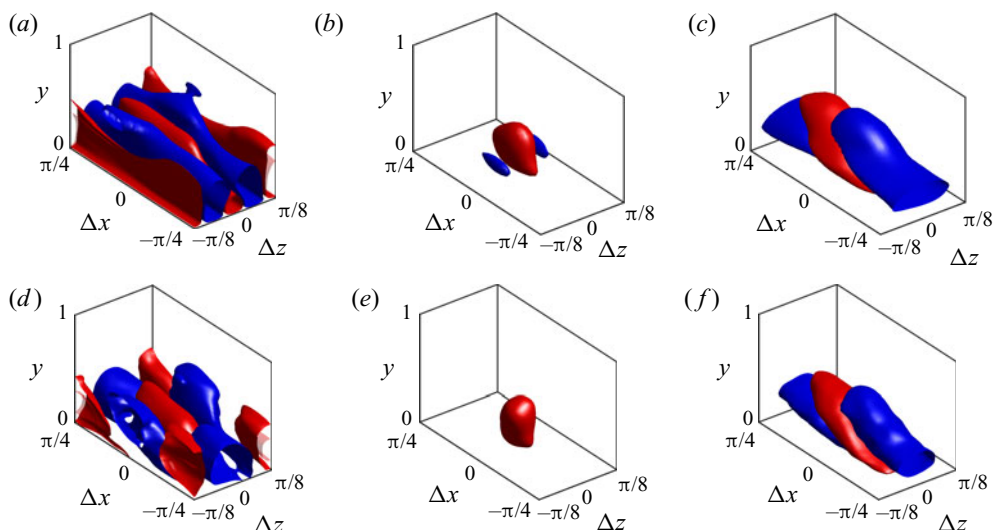


Figure 11. Correlations (a,d)  $C_{uu}$ , (b,e)  $C_{vv}$  and (c,f)  $C_{wv}$  conditioned to low-forcing-intensity events for the buffer layer (a–c) and log layer (d–f). The isosurfaces are 0.1 (red) and  $-0.04$  (blue).

of drag increase in active and passive control (García-Mayoral & Jiménez 2011, 2012; Toedtli, Yu & McKeon 2019), which is consistent with our observation that these are precursor events to generation of the principal resolvent forcing term that is crucial in generating and self-sustaining turbulence.

## 5. Conclusions

We have studied the SSP of wall-bounded turbulence in the buffer and log layers with special emphasis on the nonlinear mechanisms involved in vortex regeneration. For this purpose, we have utilised resolvent analysis to identify the most amplified nonlinear term in the incompressible Navier–Stokes equations and studied the effect of this term on numerical simulations of turbulent channel flow tailored to study isolated structures in the buffer and log layer.

Simulations of the minimal channel for the buffer and log layer with a fixed mean streamwise velocity profile were performed to isolate the structures at a prescribed scale. The most amplified nonlinear term corresponding to the most energetic wavenumber was then computed from the resolvent analysis using the mean velocity profile of the minimal channel simulations. The identified mode was removed from the nonlinear term of the corresponding simulation for a minimal channel simulation with a fixed mean velocity profile at each time step. This is made possible by the orthonormality of the resolvent modes, which provides an orthonormal basis for the nonlinear term to be projected onto. We have shown that the removal of the principal forcing mode leads to a reduction of turbulence in the flow. We also applied the removal method for subsequent forcing modes as well as non-fundamental wavenumbers instead and observed only a marginal decrease in the turbulence intensities, which reinstates the principal forcing mode for the fundamental wavenumber as the most amplified, and thus the most important, component of the nonlinear term. The diminished effect on the log layer is attributed to the multi-scale nature of high-Reynolds-number turbulence due to the more complicated interaction between various scales.

Finally, we identified the coherent structures that, through the nonlinear interaction, form the principal forcing mode. The identified structures are in the form of spanwise-sheared spanwise rolls and oblique streaks for both the buffer and log layer. The interaction of the two components highlighted here regenerates streamwise vortices, which through the lift-up mechanism amplifies streamwise streaks. These streamwise streaks break down, spawning new generations of meandering streaks and spanwise rolls, completing the SSP. The similarities in the structures identified for the buffer and log layer highlight the similarity of the nonlinear process in the SSP of the two cases.

This new technique allows the analysis of nonlinear mechanisms by combining resolvent analysis with numerical simulations of fully nonlinear Navier–Stokes equations in a realistic turbulent flow. The results show that the nonlinear mechanism of the buffer and log layer are driven by similar structures and that, without these structures present in the flow, turbulence intensity is significantly reduced. The findings corroborate previous studies on nonlinear interaction of the SSP and allow the characterisation of the underlying quadratic interactions in the SSP in the buffer and log layer of wall-bounded turbulence using resolvent analysis. The study also supports the hypothesis that the SSP in the buffer and log layer are similar by showing the similarities in the form of the principal forcing mode as well as the structures of the flow correlations conditioned to high-forcing-intensity events that lead to the generation of the principal forcing mode.

**Acknowledgements.** This work was funded in part by the Coturb programme of the European Research Council (ERC-2014.AdG-669505) during the 2017 Coturb Turbulence Summer Workshop at the Universidad Politécnica de Madrid. B.J.M. is grateful for the support of ONR under N00014-17-1-3022. A.L.-D. acknowledges the support of NASA under NNX15AU93A and of ONR under N00014-17-1-2310. The authors thank Professor J. Jiménez, Dr Y. Kwon and Dr A. Guseva for their insightful comments.

**Declaration of interests.** The authors report no conflict of interest.

#### Author ORCIDs.

-  H. Jane Bae <http://orcid.org/0000-0001-6789-6209>;
-  A. Lozano-Durán <http://orcid.org/0000-0001-9306-0261>;
-  Beverley J. McKeon <http://orcid.org/0000-0003-4220-1583>.

#### REFERENCES

- ADRIAN, R.J. 2007 Hairpin vortex organization in wall turbulence. *Phys. Fluids* **19** (4), 041301.
- AGOSTINI, L. & LESCHZINER, M. 2017 Spectral analysis of near-wall turbulence in channel flow at  $Re_\tau = 4200$  with emphasis on the attached-eddy hypothesis. *Phys. Rev. Fluids* **2** (1), 014603.
- AGOSTINI, L. & LESCHZINER, M. 2019 The connection between the spectrum of turbulent scales and the skin-friction statistics in channel flow at  $Re_\tau \approx 1000$ . *J. Fluid Mech.* **871**, 22–51.
- ALIZARD, F. 2015 Linear stability of optimal streaks in the log-layer of turbulent channel flows. *Phys. Fluids* **27** (10), 105103.
- ANDERSSON, P., BRANDT, L., BOTTARO, A. & HENNINGSON, D.S. 2001 On the breakdown of boundary layer streaks. *J. Fluid Mech.* **428**, 29–60.
- BAE, H.J. & LOZANO-DURÁN, A. 2019 A minimal flow unit of the logarithmic layer in the absence of near-wall eddies and large scales. In *Center for Turbulence Research – Annual Research Briefs*, pp. 247–254. Stanford University.
- BAE, H.J., LOZANO-DURÁN, A., BOSE, S.T. & MOIN, P. 2018 Turbulence intensities in large-eddy simulation of wall-bounded flows. *Phys. Rev. Fluids* **3**, 014610.
- BAE, H.J., LOZANO-DURÁN, A., BOSE, S.T. & MOIN, P. 2019 Dynamic slip wall model for large-eddy simulation. *J. Fluid Mech.* **859**, 400–432.
- BAE, H.J. & MCKEON, B.J. 2020 Characterization of vortex regeneration mechanism in the self-sustaining process of wall-bounded flows using resolvent analysis. *J. Phys.: Conf. Ser.* **1522**, 012001.
- BATCHELOR, G.K. & PROUDMAN, I. 1954 The effect of rapid distortion of a fluid in turbulent motion. *Q. J. Mech. Appl. Maths* **7** (1), 83–103.

- BLACKWELDER, R.F. & ECKELMANN, H. 1979 Streamwise vortices associated with the bursting phenomenon. *J. Fluid Mech.* **94** (3), 577–594.
- BUTLER, K.M. & FARRELL, B.F. 1993 Optimal perturbations and streak spacing in wall-bounded turbulent shear flow. *Phys. Fluids A* **5** (3), 774–777.
- CAMBON, C. & SCOTT, J.F. 1999 Linear and nonlinear models of anisotropic turbulence. *Annu. Rev. Fluid Mech.* **31** (1), 1–53.
- CASSINELLI, A., DE GIOVANETTI, M. & HWANG, Y. 2017 Streak instability in near-wall turbulence revisited. *J. Turbul.* **18** (5), 443–464.
- CHENG, C., LI, W., LOZANO-DURÁN, A. & LIU, H. 2019 Identity of attached eddies in turbulent channel flows with bidimensional empirical mode decomposition. *J. Fluid Mech.* **870**, 1037–1071.
- CHORIN, A.J. 1968 Numerical solution of the Navier–Stokes equations. *Maths Comput.* **22** (104), 745–762.
- COSSU, C. & HWANG, Y. 2017 Self-sustaining processes at all scales in wall-bounded turbulent shear flows. *Phil. Trans. R. Soc. Lond. A* **375** (2089), 20160088.
- DEL ALAMO, J.C. & JIMÉNEZ, J. 2003 Spectra of the very large anisotropic scales in turbulent channels. *Phys. Fluids* **15** (6), L41–L44.
- DEL ALAMO, J.C. & JIMÉNEZ, J. 2006 Linear energy amplification in turbulent channels. *J. Fluid Mech.* **559**, 205–213.
- FARRELL, B.F., GAYME, D.F. & IOANNOU, P.J. 2017 A statistical state dynamics approach to wall turbulence. *Phil. Trans. R. Soc. Lond. A* **375** (2089), 20160081.
- FARRELL, B.F. & IOANNOU, P.J. 1993 Optimal excitation of three-dimensional perturbations in viscous constant shear flow. *Phys. Fluids A* **5** (6), 1390–1400.
- FARRELL, B.F., IOANNOU, P.J., JIMÉNEZ, J., CONSTANTINOU, N.C., LOZANO-DURÁN, A. & NIKOLAIDIS, M.-A. 2016 A statistical state dynamics-based study of the structure and mechanism of large-scale motions in plane Poiseuille flow. *J. Fluid Mech.* **809**, 290–315.
- FLORES, O. & JIMÉNEZ, J. 2010 Hierarchy of minimal flow units in the logarithmic layer. *Phys. Fluids* **22** (7), 071704.
- GARCÍA-MAYORAL, R. & JIMÉNEZ, J. 2011 Hydrodynamic stability and breakdown of the viscous regime over riblets. *J. Fluid Mech.* **678**, 317–347.
- GARCÍA-MAYORAL, R. & JIMÉNEZ, J. 2012 Scaling of turbulent structures in riblet channels up to  $Re_\tau \approx 550$ . *Phys. Fluids* **24** (10), 105101.
- HAMILTON, J.M., KIM, J. & WALEFFE, F. 1995 Regeneration mechanisms of near-wall turbulence structures. *J. Fluid Mech.* **287**, 317–348.
- HELLSTRÖM, L.H.O., GANAPATHISUBRAMANI, B. & SMITS, A.J. 2016 Coherent structures in transitional pipe flow. *Phys. Rev. Fluids* **1** (2), 024403.
- HOYAS, S. & JIMÉNEZ, J. 2006 Scaling of the velocity fluctuations in turbulent channels up to  $Re_\tau = 2003$ . *Phys. Fluids* **18** (1), 011702.
- HUNT, J.C.R. & CARRUTHERS, D.J. 1990 Rapid distortion theory and the ‘problems’ of turbulence. *J. Fluid Mech.* **212**, 497–532.
- HWANG, Y. & BENGANA, Y. 2016 Self-sustaining process of minimal attached eddies in turbulent channel flow. *J. Fluid Mech.* **795**, 708–738.
- HWANG, Y. & COSSU, C. 2010 Self-sustained process at large scales in turbulent channel flow. *Phys. Rev. Lett.* **105** (4), 044505.
- HWANG, Y. & COSSU, C. 2011 Self-sustained processes in the logarithmic layer of turbulent channel flows. *Phys. Fluids* **23** (6), 061702.
- HWANG, J. & SUNG, H. 2018 Wall-attached structures of velocity fluctuations in a turbulent boundary layer. *J. Fluid Mech.* **856**, 958–983.
- JIMÉNEZ, J. 2012 Cascades in wall-bounded turbulence. *Annu. Rev. Fluid Mech.* **44**, 27–45.
- JIMÉNEZ, J. 2013 Near-wall turbulence. *Phys. Fluids* **25** (10), 101302.
- JIMÉNEZ, J. 2015 Direct detection of linearized bursts in turbulence. *Phys. Fluids* **27** (6), 065102.
- JIMÉNEZ, J. 2018 Coherent structures in wall-bounded turbulence. *J. Fluid Mech.* **842**, P1.
- JIMÉNEZ, J. & MOIN, P. 1991 The minimal flow unit in near-wall turbulence. *J. Fluid Mech.* **225**, 213–240.
- JIMÉNEZ, J. & PINELLI, A. 1999 The autonomous cycle of near-wall turbulence. *J. Fluid Mech.* **389**, 335–359.
- JOVANOVIĆ, M.R. & BAMIEH, B. 2005 Componentwise energy amplification in channel flows. *J. Fluid Mech.* **534**, 145–183.
- KAWAHARA, G., JIMÉNEZ, J., UHLMANN, M. & PINELLI, A. 2003 Linear instability of a corrugated vortex sheet—a model for streak instability. *J. Fluid Mech.* **483**, 315–342.
- KAWAHARA, G. & KIDA, S. 2001 Periodic motion embedded in plane Couette turbulence: regeneration cycle and burst. *J. Fluid Mech.* **449**, 291–300.
- KIM, J. & LIM, J. 2000 A linear process in wall-bounded turbulent shear flows. *Phys. Fluids* **12** (8), 1885–1888.

- KLEBANOFF, P.S., TIDSTROM, K.D. & SARGENT, L.M. 1962 The three-dimensional nature of boundary-layer instability. *J. Fluid Mech.* **12** (1), 1–34.
- KLINE, S.J., REYNOLDS, W.C., SCHRAUB, F.A. & RUNSTADLER, P.W. 1967 The structure of turbulent boundary layers. *J. Fluid Mech.* **30** (4), 741–773.
- LANDAHL, M.T. 1975 Wave breakdown and turbulence. *SIAM J. Appl. Maths* **28** (4), 735–756.
- LEONARD, A. 1975 Energy cascade in large-eddy simulations of turbulent fluid flows. *Adv. Geophys.* **18**, 237–248.
- LIN, C.C. 1944 *On the Stability of Two-Dimensional Parallel Flows*. Guggenheim Aeronautical Laboratory.
- LOZANO-DURÁN, A. & BAE, H.J. 2016 Turbulent channel with slip boundaries as a benchmark for subgrid-scale models in LES. In *Center for Turbulence Research – Annual Research Briefs*, pp. 97–103. Stanford University.
- LOZANO-DURÁN, A. & BAE, H.J. 2019a Characteristic scales of Townsend’s wall-attached eddies. *J. Fluid Mech.* **868**, 698–725.
- LOZANO-DURÁN, A. & BAE, H.J. 2019b Error scaling of large-eddy simulation in the outer region of wall-bounded turbulence. *J. Comput. Phys.* **392**, 532–555.
- LOZANO-DURÁN, A., BAE, H.J. & ENCINAR, M.P. 2020 Causality of energy-containing eddies in wall turbulence. *J. Fluid Mech.* **882**, A2.
- LOZANO-DURÁN, A., FLORES, O. & JIMÉNEZ, J. 2012 The three-dimensional structure of momentum transfer in turbulent channels. *J. Fluid Mech.* **694**, 100–130.
- LOZANO-DURÁN, A. & JIMÉNEZ, J. 2014 Time-resolved evolution of coherent structures in turbulent channels: characterization of eddies and cascades. *J. Fluid Mech.* **759**, 432–471.
- MALKUS, W.V.R. 1956 Outline of a theory of turbulent shear flow. *J. Fluid Mech.* **1** (5), 521–539.
- MARUSIC, I., MCKEON, B.J., MONKEWITZ, P.A., NAGIB, H.M., SMITS, A.J. & SREENIVASAN, K.R. 2010 Wall-bounded turbulent flows at high Reynolds numbers: recent advances and key issues. *Phys. Fluids* **22** (6), 065103.
- MARUSIC, I. & MONTY, J.P. 2019 Attached eddy model of wall turbulence. *Annu. Rev. Fluid Mech.* **51**, 49–74.
- MARUSIC, I., MONTY, J.P., HULTMARK, M. & SMITS, A.J. 2013 On the logarithmic region in wall turbulence. *J. Fluid Mech.* **716**, R3.
- MCKEON, B.J. 2017 The engine behind (wall) turbulence: perspectives on scale interactions. *J. Fluid Mech.* **817**, P1.
- MCKEON, B.J. 2019 Self-similar hierarchies and attached eddies. *Phys. Rev. Fluids* **4** (8), 082601.
- MCKEON, B.J. & SHARMA, A.S. 2010 A critical-layer framework for turbulent pipe flow. *J. Fluid Mech.* **658**, 336–382.
- MENEVEAU, C. & MARUSIC, I. 2013 Generalized logarithmic law for high-order moments in turbulent boundary layers. *J. Fluid Mech.* **719**, R1.
- MOARREF, R., SHARMA, A.S., TROPP, J.A. & MCKEON, B.J. 2013 Model-based scaling of the streamwise energy density in high-Reynolds-number turbulent channels. *J. Fluid Mech.* **734**, 275–316.
- MORRA, P., SEMERARO, O., HENNINGSON, D. & COSSU, C. 2019 On the relevance of Reynolds stresses in resolvent analyses of turbulent wall-bounded flows. *J. Fluid Mech.* **867**, 969–984.
- ORLANDI, P. 2000 *Fluid Flow Phenomena: A Numerical Toolkit*. Springer.
- ORR, W.M.F. 1907 The stability or instability of the steady motions of a perfect liquid and of a viscous liquid. Part II: a viscous liquid. In *Proceedings of the Royal Irish Academy (A)*, vol. 27, pp. 69–138. JSTOR.
- PANTON, R.L. 1997 *Self-Sustaining Mechanisms of Wall Turbulence*. Computational Mechanics.
- PANTON, R.L. 2001 Overview of the self-sustaining mechanisms of wall turbulence. *Prog. Aerosp. Sci.* **37** (4), 341–383.
- PARK, J., HWANG, Y. & COSSU, C. 2011 On the stability of large-scale streaks in turbulent Couette and Poiseuille flows. *C. R. Méc.* **339** (1), 1–5.
- PERRY, A.E. & CHONG, M.S. 1982 On the mechanism of wall turbulence. *J. Fluid Mech.* **119**, 173–217.
- PUJALS, G., GARCÍA-VILLALBA, M., COSSU, C. & DEPARDON, S. 2009 A note on optimal transient growth in turbulent channel flows. *Phys. Fluids* **21** (1), 015109.
- REYNOLDS, W.C. & HUSSAIN, A.K.M.F. 1972 The mechanics of an organized wave in turbulent shear flow. Part 3. Theoretical models and comparisons with experiments. *J. Fluid Mech.* **54** (2), 263–288.
- ROBINSON, S.K. 1991 Coherent motions in the turbulent boundary layer. *Annu. Rev. Fluid Mech.* **23** (1), 601–639.
- ROZEMA, W., BAE, H.J., MOIN, P. & VERSTAPPEN, R. 2015 Minimum-dissipation models for large-eddy simulation. *Phys. Fluids* **27** (8), 085107.
- SCHOPPA, W. & HUSSAIN, F. 2002 Coherent structure generation in near-wall turbulence. *J. Fluid Mech.* **453**, 57–108.

## Nonlinear mechanism of the SSP of wall-bounded flows

- SMITH, C.R. & METZLER, S.P. 1983 The characteristics of low-speed streaks in the near-wall region of a turbulent boundary layer. *J. Fluid Mech.* **129**, 27–54.
- SMITS, A.J., MCKEON, B.J. & MARUSIC, I. 2011 High-Reynolds number wall turbulence. *Annu. Rev. Fluid Mech.* **43**, 353–375.
- SWEARINGEN, J.D. & BLACKWELDER, R.F. 1987 The growth and breakdown of streamwise vortices in the presence of a wall. *J. Fluid Mech.* **182**, 255–290.
- SYMON, S., ILLINGWORTH, S.J. & MARUSIC, I. 2020 Energy transfer in turbulent channel flows and implications for resolvent modelling. [arXiv:2004.13266](https://arxiv.org/abs/2004.13266).
- TOEDTLI, S.S., YU, C.H. & MCKEON, B.J. 2019 Structural and spectral analysis of varying phase opposition control in turbulent channel flow. In *Proceedings of Turbulence and Shear Flow Phenomena 2019*, 37. University of Southampton.
- TOWNSEND, A.A. 1976 *The Structure of Turbulent Shear Flow*. Cambridge University Press.
- TUERKE, F. & JIMÉNEZ, J. 2013 Simulations of turbulent channels with prescribed velocity profiles. *J. Fluid Mech.* **723**, 587–603.
- WALEFFE, F. 1995 Transition in shear flows. Nonlinear normality versus non-normal linearity. *Phys. Fluids* **7** (12), 3060–3066.
- WALEFFE, F. 1997 On a self-sustaining process in shear flows. *Phys. Fluids* **9** (4), 883–900.
- WALEFFE, F. 1998 Three-dimensional coherent states in plane shear flows. *Phys. Rev. Lett.* **81** (19), 4140–4143.
- WALEFFE, F. 2001 Exact coherent structures in channel flow. *J. Fluid Mech.* **435**, 93–102.
- WALEFFE, F. 2003 Homotopy of exact coherent structures in plane shear flows. *Phys. Fluids* **15** (6), 1517–1534.
- WRAY, A.A. 1990 Minimal-storage time advancement schemes for spectral methods. *NASA Tech. Rep.* MS 202